McNair Research Journal SJSU

Volume 19 *Spring 2023* Article 9

2023

A Cost-Effective and Smart Sensing Tissue-like Testbed for Surgical Training

Lysette Zaragoza

Follow this and additional works at: https://scholarworks.sjsu.edu/mcnair

Part of the Biochemistry Commons, Biotechnology Commons, and the Medicine and Health Sciences Commons

Recommended Citation
Zaragoza, Lysette (2023) "A Cost-Effective and Smart Sensing Tissue-like Testbed for Surgical Training," *McNair Research Journal SJSU*: Vol. 19 , Article 9.
https://doi.org/10.31979/mrj.2023.1909 https://scholarworks.sjsu.edu/mcnair/vol19/iss1/9

This Article is brought to you for free and open access by SJSU ScholarWorks. It has been accepted for inclusion in McNair Research Journal SJSU by an authorized editor of SJSU ScholarWorks. For more information, please contact scholarworks@sjsu.edu.

Lysette Zaragoza

Major:
Mechanical Engineering
Minor: Robotics

Mentor:
Dr. Jin Liang

Co-Authors:
Joshua Billmann, Eric Barlog, Gaojian Huang, Egbe-Etu Etu,

A Cost-Effective and Smart Sensing Tissue-like Testbed for Surgical Training

Biography

Lysette is a senior graduating during Spring 2023 with a Bachelor of Science in mechanical engineering and a minor in robotics. She will be the first person in her family to become an engineer. Through her undergraduate career, she has had three research internships at the University of Missouri, Florida A&M University, and Contra Costa College as well as one industry internship at Lockheed Martin. This engineering experience has spanned diverse fields with a focus on manufacturing and robotics in both the biomedical and aerospace areas. Beyond academics, she is passionate about uplifting others who are underrepresented in engineering such as through her current role as the professional development director in the SJSU Society of Women Engineers. She aims to continue contributing to this cause after graduating and entering the field.

Abstract

A low-cost tissue-like testbed with six nodes of varying stiffness was developed for surgical training to provide pressure and force feedback data through image reception to human operators. Using SolidWorks, a 3D model of the box trainer housing was created. A pad for the distribution of smartsensing nodes and microcontroller connections was designed with open spaces for the respective components. The pad was 3D-printed with PLA filament. Flat piezoelectric pressure sensors were fabricated with conductive materials and velostat sensor material. Using static and dynamic analyses, three top sensors were chosen to be used in three pressure sensing nodes. A calibration process was performed on the pressure sensors to find the linear relationship between voltage and pressure, which was then used to create a conversion equation for each sensor. These equations were used to collect data at the three pressure sensing nodes on the silicone testbed pad. Conductive TPU filament was used to 3D-print vertical force sensors, which were designed using SolidWorks. The force sensors were calibrated with a squeezing mechanism to find a relationship between voltage and force and to subsequently develop a conversion equation for each sensor. We used these equations to collect force data from the three force sensing nodes on the testbed pad. Through static and dynamic analyses, the force sensors were found to be functional, but to need improvements in accuracy. The mechatronic system was designed and developed to integrate all six sensors and to collect data from the testbed pad using an Arduino microcontroller. The flat pressure and vertical force sensors were embedded in each node to measure the pressure and force that occurs during the deformation of the six nodes. Data was collected and imported into MATLAB. This data was used in displaying pressure and force mapping of the nodes over a live video of the silicone pad. Pressure and force mapping was realized by drawing color-coded circles on each of the six nodes that correspond to a range of force or pressure values. From this development, the surgical testbed provides multi-stiffness tissue training with live pressure and force mapping overlaid on a live video of the emulated surgical field.

https://scholarworks.sjsu.edu/mcnair/vol19/iss1/9
DOI: 10.31979/mrj.2023.1909

1 Introduction

1.1 Significance of advancing technologies in Minimal Invasive Surgery (MIS)

Minimally invasive surgery (MIS) aims to perform operations through only a few small incisions rather than large incisions typical of traditional, open surgery [1]. This results in reduced pain after the surgery and shorter recovery time for the patient. Most importantly, MIS significantly reduces medical risks such as blood loss, post-operative bleeding, internal organ exposure to contaminants, and post-operative infections [2]. Therefore, over the last three decades, minimally invasive surgery has been universally accepted for a wide range of surgical applications. The acceptance of MIS has led to significant reductions in morbidity, readmission, as well as reoperation [3]. For example, in the case of endometrial cancer treatment, minimally invasive surgery was compared with open surgery and it was found that MIS had decreased odds in several areas such as n=247 versus n=347 in major complications, n=238 versus n=269 in readmission, n=80 versus n=93 in reoperation, and n=20 versus n=41 in death. In the application of small bowel resections, MIS is underutilized as it is only applied to 9% of patients receiving the procedure [4]. However, when compared to open surgery in this application, MIS had a mortality rate of 2.9% versus 8.2% and a morbidity rate of 1.7% versus 4.3%. Therefore, the utilization of minimally invasive surgery has proven to make a significant impact on surgical success and outcomes in a wide span of surgical specialties.

The primary setup of minimally invasive surgery procedures consists of contact with the surgical field through small incisions, a laparoscope with a light and camera to get video imaging of the surgical field, a 2D video monitor to view the surgical field, and other long surgical instruments to perform the procedure, as shown in Figure 1. Compared to open surgery, MIS requires a unique set of technical skills that form steep learning curves that doctors must train through [5]. During MIS procedures, surgeons must utilize a 2D video screen to visualize the surgical field, which creates impairments in depth perception. Additionally, switching from

direct hand contact with the surgical field to contact using rigid laparoscopic instruments leads to a lack of tactile feedback. Lastly, using the long laparoscopic surgery instruments creates an effect called the fulcrum effect that amplifies tremors in the surgeon's hands. Therefore, the most important component for the successful implementation of minimally invasive procedures in the medical field is MIS training to account for the adaptation of these new skills.

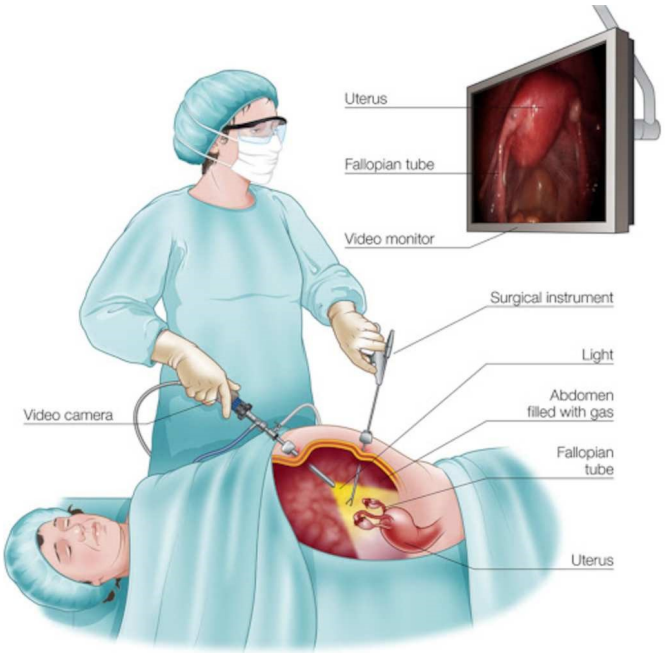

Fig. 1: Minimally invasive surgery setup. [6]

1.2 Current Surgical Training Solutions

Physical Box Trainers Because minimally invasive surgery requires the acquisition of niche technical skills, adequate training is necessary for skill development under the circumstances of impaired depth perception, the lack of tactile feedback, and the long instruments that are required to be used [5]. Therefore, it is important that training is grounded in surgical simulation, rather than the traditional apprentice training model, and that the simulation emulates the MIS circumstances as much as possible. The

https://scholarworks.sjsu.edu/mcnair/vol19/iss1/9
DOI: 10.31979/mrj.2023.1909

foundational method of MIS training is the box trainer. The box trainer typically consists of a box containing holes where the trocar instrument can be inserted with the goal of simulating the surgical environment such as the abdominal cavity [2]. They can be used with the laparoscopic instruments and contain a camera to replicate the endoscopic camera that provides visual access via a 2D video. Typically, these box trainers allow for practicing the manipulation of objects like pegs or the practice of simple cutting and suturing tasks.

In an effort to standardize the training and evaluation of laparoscopic training, the Fundamentals of Laparoscopic Surgery (FLS) program was created. It trains for both cognitive and psychomotor skills. The psychomotor skills are trained through a box trainer that allows for the practice of tying knots, picking, precise cutting, suturing, and transferring between hands. The box trainer itself serves as a traditional box trainer that includes an opening on one end of the box and a white color to allow for light to enter the simulated training area [7]. The components utilized as emulation of the surgical field for the trainee to practice on are a peg board with several triangles for picking and placing, gauze pads with drawn shapes to practice precise cutting, a block to practice suturing with knot tying, and fake organs made from foam to practice creating a ligating loop. All of these tools are used in a strict evaluation of the trainee's ability to perform these tasks. Therefore, this FLS box trainer provides an established foundation of motor skills that need to be tested for laparoscopic surgery. However, it does not provide any further advanced feedback such as the interactions with replicas of human tissue and the amount of force or pressure that is being applied. Therefore, there is a clinical need for surgical trainers that emulate the variation that exists in tissue stiffnesses within the human body and that provide force and pressure feedback to train in control for delicate tasks.

Fig. 2: Fundamentals of Laparoscopic Surgery (FLS) Trainer [8]

The traditional box trainer is a common training method due to its widespread implementation under the Fundamentals of Laparoscopic Surgery (FLS) program [2]. Their benefit is that they are on the cheap side of MIS trainers, coming out to as low as $180 for off-brand box trainers [9] and as high as $1,199 for the official FLS program box trainer [10]. On the other end of the spectrum, the most expensive box trainers such as the Lap-X Box Laparoscopy Trainer [11] and the Lap-X VR Simulator [12] provide more advanced skills training in areas such as suturing and more advanced visual feedback as well as more information such as the amount of mistakes and the duration of the skills task. However, they are very expensive at $2,950 and $8,950, respectively, which affects their accessibility for surgical training. Most importantly, all of these surgical trainers presented from the market lack a key component of MIS training: pressure and force feedback, which is necessary for the adaptation of indirect surgical contact via laparoscopic instruments. Overall, current box trainer solutions only allow for the practice of generic skills without pressure or force feedback while the more adequate virtual reality simulation methods are expensive, making adequate laparoscopic training relatively inaccessible.

The inclusion of sensor-based feedback in surgical box trainers is a novel feature, for which the current research has performed varying design

https://scholarworks.sjsu.edu/mcnair/vol19/iss1/9
DOI: 10.31979/mrj.2023.1909

configurations [13]. These studies have explored the added feature of integrating sensors into the box trainer apparatus as well as replicating the abdomen instead of relying on generic skills accessories. Sensors are directly integrated into the emulated surgical field such as a tissue pad. One study aimed to build a box trainer that is capable of measuring the forces of interactions between the replica tissue and the instrument along with visual feedback regarding the forces in the camera imaging. The platform to measure these forces, or the Force Platform, was created with the Optoelectronic 6D mouse that is on the market and an added 3-spring mechanical platform to increase the range of forces [14]. Coding in C++ was used to set up and calibrate the mouse for captivating vectors in 6 degrees of freedom: rotation in the x, y, and z directions as well as translation in the x, y, and z directions. In the overall apparatus, artificial tissue was attached to the top of the force sensor and had two markings for the incision point and the direction of the incision [13]. A laparoscopic camera was also fixed to the inside of the box. Adequate lighting was acquired through placing 8 white LED lights near the lens of the camera to create a beam of white light. Additionally, MATLAB was used to create the user interface that displayed the camera images and to record the data in real time. In this interface, an arrow is overlaid into the image to represent the magnitude and direction given by the exerted force of the user. Its color also changes depending on if it is approaching the maximum force allowed for that particular task. This system serves as a model that can objectively assess trainees through force sensing and visualization in laparoscopic box trainers. From this study, we want to further implement the idea of sensor integration by embedding force and pressure sensors within silicone tissue that the trainee interacts with. However, due to our goal of cost-effectiveness, we aim to utilize cheaper options than purchasing advanced platforms, including fabricating our own pressure and force sensors, using 3D-printing, and using silicone materials. Another aspect we want to take forward from this study is the concept of visual feedback for the trainee based on how much pressure or force they are applying. However, instead of utilizing an arrow to show the amount of force, we want to use a color-based format of pressure and force mapping to show how the pressure or force is changing within specific ranges at each node. This gives a more in-

depth understanding through two different sets of sensor data that come from sensors and sensing nodes that are specifically fabricated to provide feedback on tissue-based interaction.

1.3 Clinical Needs for Surgical Training

During minimally invasive surgery training, the current training assessments focus primarily on movement efficiency and completion time of tasks involving grasping and positioning [14]. However, there is a need for assessing performance when it comes to one of the most important skills in surgery: performing delicate tasks. The assessment requires the measurement of parameters involving the interaction forces that occur when the tool makes contact with the tissue. With force and pressure feedback missing from current training solutions, it is shown that MIS has a clinical need for the training of adequate force and pressure control in order to prevent surgical damages or complications.

In addition to the lack of force and pressure feedback in current surgical trainers, accessibility to MIS training is a significant clinical need that exists in the medical community [15]. Although it is known that skills developed from a simulated environment lead to improving performance within operating rooms, access to MIS training equipment is limited. In fact, most surgeons in training end up developing their surgical skills for MIS through practice from live patient procedures. In a global study of MIS training accessibility over a wide range of surgical areas, it was found that out of 292 survey responses, 34% had access to a surgical simulation trainer during their working hours and only 20% had access outside of working time. Within the previous 12 months, 46% did not use a surgical simulator at all while 19% reported use for more than 6 hours in that year. This shows a severe lack of training in minimally invasive surgery, which stems from high stress working time limiting training time and cost as a barrier to obtaining surgical simulators. Beyond the lack of usage, there is agreement amongst medical professionals where 79% agreed that competency should be shown on a simulator prior to performing procedures. Moreover, 75% believe that take-home simulation trainers for MIS can play an important role in training and 86% support the usage of simulators for warm-up while only 26% are doing this. Therefore, the clinical need for accessibility is

https://scholarworks.sjsu.edu/mcnair/vol19/iss1/9
DOI: 10.31979/mrj.2023.1909

prevalent in the medical community and points towards a solution via cost and home-accessible surgical trainers.

1.4 Application of the Test bed for Robotic MIS

A robot with human intervention is called teleoperation [16]. Teleoperation provides a bidirectional interaction between humans and robots via enhanced perception and motion by integrating human intelligence with the robot's advantages over the constraint of distance [17–23]. Studies on bidirectional teleoperation system manipulation have largely focused on how to drive the follower robot more efficiently and robustly with various control method, such as adaptive control [20], predictive control [19], sliding mode control [17], and combinations thereof. In large part, the aims are on simplifying the workspace and adding predefined constraints.

Improving the bilateral human-robot interaction in real-time is a necessary, yet challenging, aspect of teleoperated surgical training, especially in a complex workspace environment. The goal of this work is to design and develop a smart testbed for surgical training and simulation that will provide sensing feedback, pressure and force mapping and live image information for better evaluating task performance in a future application of telesurgical operation.

The introduction of robotics into minimally invasive surgery has made the procedures more precise and efficient [1]. For instance, by moving the surgeon's control of operating tools to a remote station, specially designed robotic tool arms with greater articulation and flexibility allow for a broader range of tool motion. Further, sensing of the surgeon's fine hand movements is used to stabilize the output motion of the robot and eliminate transmission of tremors from a surgeon's hand to the surgical tool [24]. Additionally, robotic implementation opens the door for haptics, or the simulation of touch interactions, to return direct force feedback back to the hands of surgeons that must interact with indirect surgical instruments [25].

Therefore, robotics plays a vital role in improving MIS procedures. With the introduction of new technology, comes the need for adaptive training. Many hospitals and medical schools have inanimate physical laparoscopy simulators for medical students and staff to practice their skills

[26]. However, these simulators are intended for traditional laparoscopy with manual tools. Given that the traditional laparoscopic experience does not translate into the different skill sets required for robotic-assisted surgery [27], traditional simulators are insufficient for adequate training in robotic laparoscopy. Furthermore, most medical students do not receive any sort of structured simulator training until postgraduate residency or later in their career. A lack of teaching of the unique skills necessary for robotic assisted surgery, in combination with the increased ability of younger people to improve their skills via robotic surgical training compared with older students further in their education or career [27], presents a convincing case for integrating a robotic-specific training program earlier in medical school. This warrants consideration of the robotic space by integrating the testbed into an overall robotic system after the development of the standalone smart-sensing testbed.

1.5 Research Objectives

To address the issue of a lack of accessible and adequate MIS training, our project aimed to create a Minimally Invasive Surgery (MIS) training bed that is both cost-effective and smart. This training bed consists of a traditional testbed box trainer that contains housing and lighting for a tissue pad as well as slots for trocar insertion and the MIS tooling. We designed and developed a smart artificial tissue pad with integrated pressure and force sensors. A USB camera was placed in a camera holder on the box trainer for live imaging of the emulated surgical field within the testbed. Fabricated pressure sensors allowed for the measurement of pressure upon interaction between the surgical instrument and three pressure sensing nodes while the force sensors did the same for three force sensing nodes. The setup also included a live video display of the tissue pad within the testbed housing. The live imaging was overlaid with pressure and force mapping of the tissue pad nodes by gathering pressure and force data from the integrated sensors. This created a surgical testbed that is portable, relatively cheap, and effective through live visual feedback.

https://scholarworks.sjsu.edu/mcnair/vol19/iss1/9
DOI: 10.31979/mrj.2023.1909

In addition to this primary focus for improving upon what is currently on the market for box trainers, the smart-sensing test bed will play a larger role within the development of robotic laparoscopic surgery. More specifically, it will be integrated into a teleoperated MIS robotic training system. The testbed will be the device practiced on by the surgeon in training and will also allow for the incorporation of various sensing feedback. Therefore, the designed testbed will be uniquely capable of playing two roles: 1) as a training bed that can be used on its own for more accessible and effective MIS training practices with pressure and force feedback via live imaging; and 2) as a testbed that can be integrated into a larger system of a telesurgical robotic training apparatus.

2 Methodology

The realization of the cost-effective, smart MIS training bed required 3 phases of design and development, which are a) mechanical design and fabrication of the testbed, b) sensor fabrication and calibration, and c) software development of the live image processing with force and pressure mapping.

Overview of the surgical training apparatus The apparatus for the cost-effective, smart-sensing surgical testbed consists of four main components:

1. Box trainer housing.
2. Pad for the distribution of nodes with integrated sensors.
3. Sensors to obtain force and pressure feedback data.

4. Live image processing with force and pressure mapping

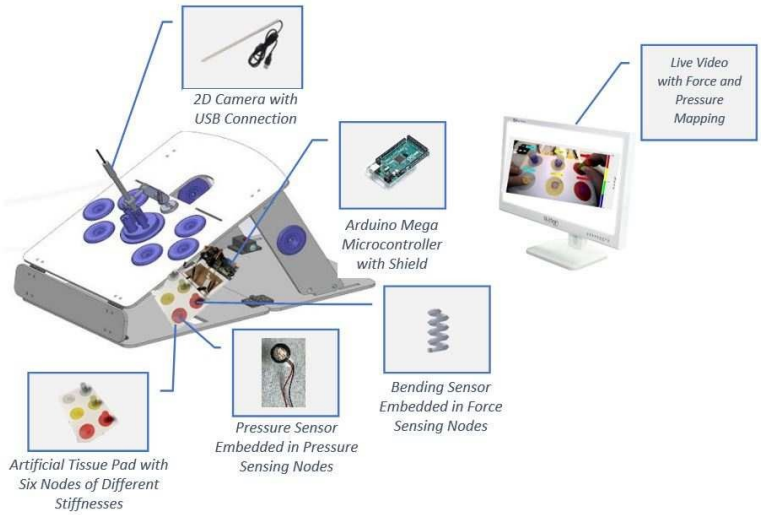

Fig. 3: Smart-sensing surgical training apparatus.

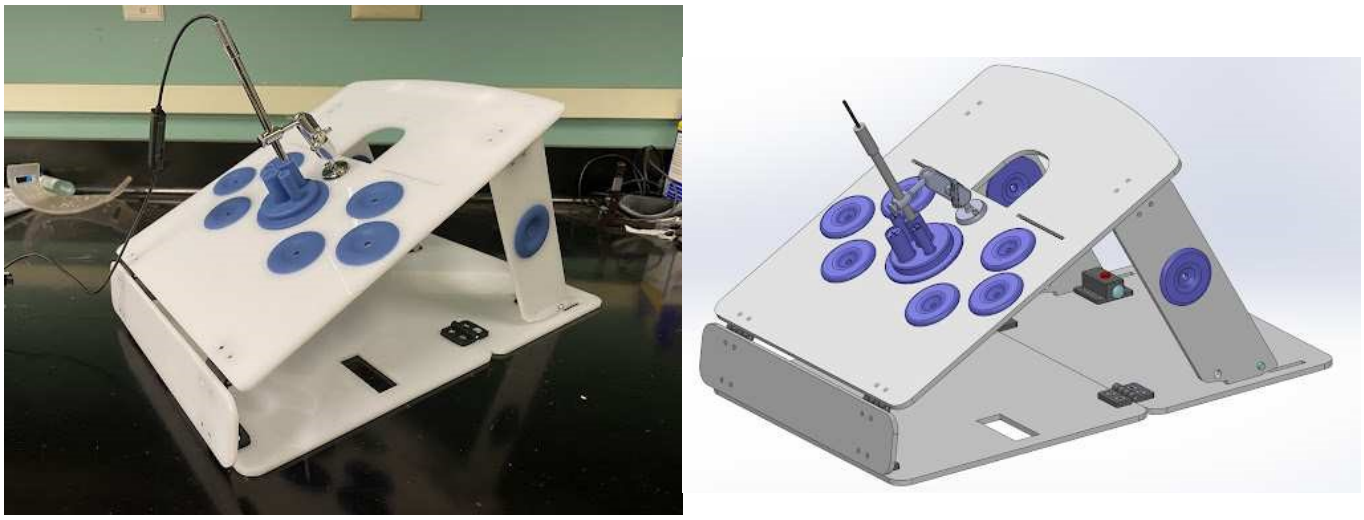

(a) (b)

Fig. 4: Box trainer (a) and 3D-modeled box trainer housing (b).

https://scholarworks.sjsu.edu/mcnair/vol19/iss1/9
DOI: 10.31979/mrj.2023.1909

The purchased box trainer serves as the foundation of the apparatus that establishes the physical space within which the apparatus resides. The pad that represents the primary surgical field consists of three multi-stiffness nodes for force sensing and three multi-stiffness nodes for pressure sensing. To practice the performance of MIS with the view of the surgical field through a video, live image processing is used to create the live video and it is overlaid with visual mapping of the force and pressure feedback data.

2.1 Mechanical design of the testbed

Box trainer housing A standard surgical box trainer was purchased from the cheapest end of the commercially available spectrum to serve as the primary housing for the surgical training bed. The box trainer was hand-measured to obtain dimensions and modeled using SolidWorks. This model allowed us to establish the dimensions of the overall testbed apparatus and the parameters within which we designed the pad as well as the surgical field inside. It also provides the feature of trocar holes for instrument insertion and a camera holder for placement of the camera that obtains the live video imaging as well as additional lighting for the pad.

Nodes for pressure sensing Pressure sensing nodes were designed with a flat circular shape consisting of an elevated buttonlike rise in the center. This shape is ideal for the primary functionality of the pressure sensing node where the user will press directly down on the node with an MIS instrument to be provided with pressure feedback. Additionally, the circular shape was designed to correspond to a circular placement section in the primary pad that holds the sensors in the surgical field.

To provide MIS training for various tissue stiffnesses in the human body, three pressure sensing nodes were fabricated with silicone materials of different stiffness. The materials, as shown in table 1, emulate fat, glandular, and vascular tissue based on their corresponding Young's Modulus. For the user to easily distinguish between the materials and their variation in pressure feedback behavior, the nodes were dyed with no color, yellow coloring, and red coloring, respectively.

Table 1: Durometer Levels, Young's Modulus, and Elastic Modulus in various types of Human Tissues for Nodes with Assigned Colors.

Durometer	Young's Modulus	Human Tissue	Assigned Color
Shoreness 00-10	10 kPa	Fat [28]	White
Shoreness 00-30	25 kPa	Glandular [29]	Yellow
Shoreness 2A	36 kPa	Vascular [30]	Red

Fabrication of the pressure sensing nodes was performed through a silicone molding process that utilized 3D-printed molds. The molds consisted of two pieces: one piece to provide a flat, circular shape with a rise in the center and another piece to provide a thin and completely flat circular shape. Both pieces were 3D-printed with PLA filament and were designed to be open on top and to have an outline of the desired shape within the mold, as shown in figure 5. A consistent process was maintained to uphold quality during the silicone molding process. This included spraying the mold with a mold release spray prior to pouring silicone into it, placing the silicone in a vacuum chamber to remove gaps in the material, pouring the silicone into the mold with a pipette to accurately fill the mold level to its height, and placing the filled mold onto the hot plate at 65 degrees to enact the curing process with a faster, more efficient time frame. Once cured, the silicone was easily removed through pulling out from the mold of both pieces.

https://scholarworks.sjsu.edu/mcnair/vol19/iss1/9
DOI: 10.31979/mrj.2023.1909

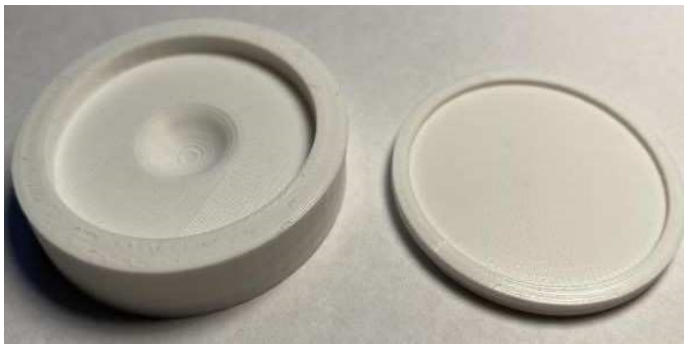

Fig. 5: Silicone molds for pressure sensing nodes.

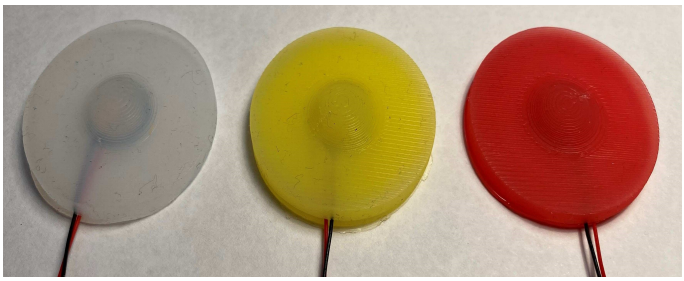

Fig. 6: Pressure sensing nodes.

The final goal of the pressure sensing node was to integrate a flat, piezoelectric pressure sensor directly below the buttonlike rise to create the node with capabilities for pressure feedback. This was achieved by sandwiching the pressure sensor between the silicone piece with the rise and the completely flat silicone piece and securing the layout with glue, producing the final pressure sensing nodes in figure 6.

Nodes for force sensing Force sensing nodes were designed with a vertical cylindrical shape and a flat circular bottom that fans out from the cylinder. This shape is compatible with the force sensing node's primary usage of being squeezed and bent by the trainee via an MIS strument to provide force feedback. The circular bottom was incorporated into the design so that the node can be placed in the corresponding circular placement within the pad for node distribution. Three force sensing nodes were fabricated with the same multi-stiffness silicone materials as the

pressure sensor nodes and were also color-coded in the same way, as shown in figure 7.

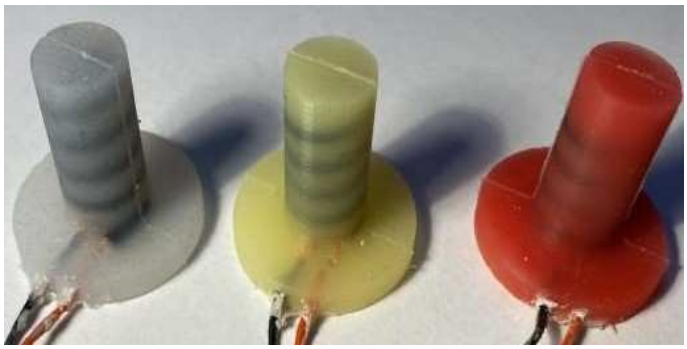

Fig. 7: Force sensing nodes.

Force sensing nodes were fabricated through close to the same silicone molding process as the pressure sensing nodes, but with a different design for the 3D-printed molds and additional steps for the integration of the vertical sensor. The mold for the force sensing node consists of two halves that create the vertical cylindrical shape with the circular bottom. The radius of the half-cylinder in each mold component was determined in order to give the slightest thickness possible past the diameter of the sensor. Prior to pouring the silicone into the mold, the two halves are screwed together and tape is placed on the flat surface of the two halves to prevent leaking. Additionally, to center and keep the vertical force sensor in place, particularly with its attached wiring, trenches were incorporated to the top of the node mold to allow for a resting placement of the wires that aligned with the extensions designed into the sensor. Clay was then used to hold the wires in place within the trenches in order to keep the sensor upright and centered during the silicone pouring and curing process.

https://scholarworks.sjsu.edu/mcnair/vol19/iss1/9
DOI: 10.31979/mrj.2023.1909

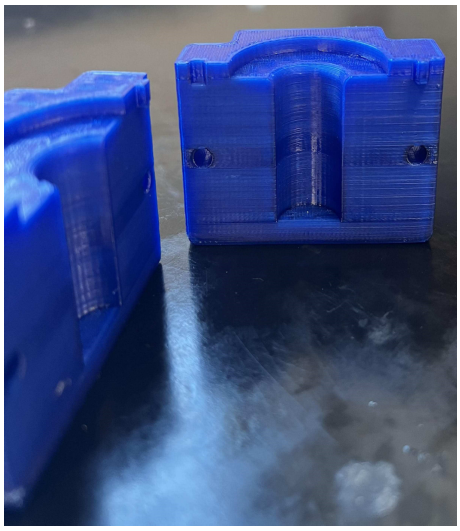

Fig. 8: Silicone molds for force sensing nodes.

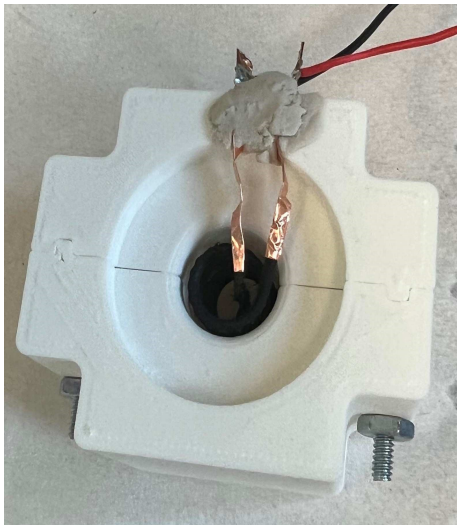

Fig. 9: Force sensor placed using clay before pouring silicone.

Pad for the distribution of pressure and force sensing nodes

To create the primary surgical field that is placed inside of the box trainer, we designed a pad in SolidWorks with a layout for the six sensors and with placements for the mechatronic components. The pad, as shown in

figure 10, was designed with a placement for the Arduino MEGA microcontroller in the back of the pad, including screw holes to hold the Arduino in place. In the front of the pad, placements were designed to hold each of the six nodes with the three pressure sensing nodes being held in the first row and the three force sensing nodes being held in the second row. The sizing of the circular placement cut-outs was designed to match the radius and height of the circular pressure nodes and the circular base of the force sensing nodes for a level fit. The pad was 3D-printed with PLA filament.

Piezoelectric pressure sensors

Piezoelectric pressure sensors were fabricated by hand through a layering technique consisting of five total materials as shown in figure 11: velostat, conductive fabric, copper tape, clear tape, and a soft elastomer material.

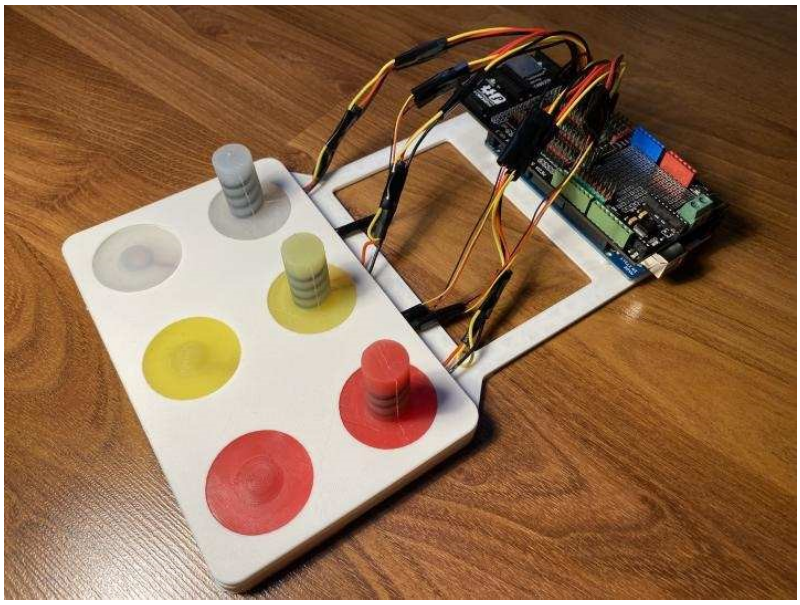

Fig. 10: Testbed pad for node distribution connected to the mechatronic set-up.

https://scholarworks.sjsu.edu/mcnair/vol19/iss1/9
DOI: 10.31979/mrj.2023.1909

The flat design of the pressure sensors was enacted due to their desired position of being placed below the pressure nodes to gather pressure feedback data as the user presses directly on them with an MIS surgical instrument.

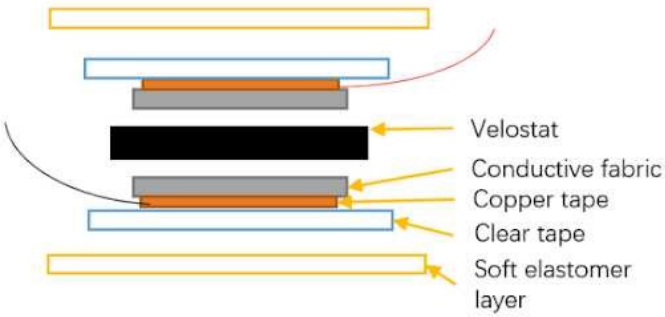

Fig. 11: Diagram of layered materials for the fabrication of piezoelectric pressure sensors.

Fig. 12: Piezoelectric pressure sensor.

Force sensors

The force sensors were designed in SolidWorks to have a vertical, cylindrical shape to match the primary use of bending and squeezing. Spirals were utilized along the vertical design to amplify the bending capability and the corresponding conductive behavior. Two ends were

designed for attaching wires as the power and ground connections. One end was designed

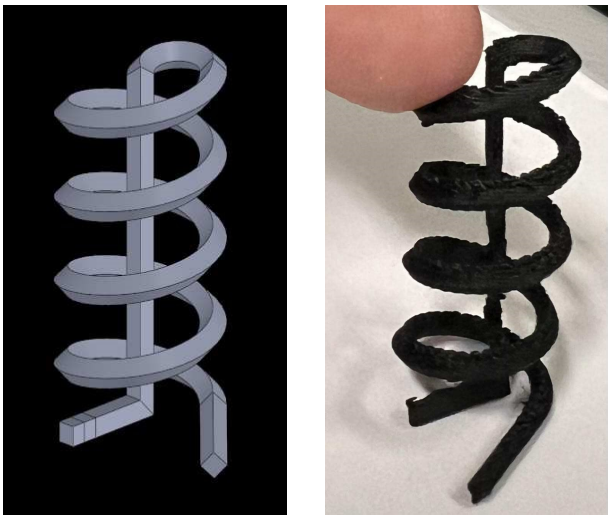

(a) (b)

Fig. 13: 3D model of force sensor (a) and 3D-printed force sensor (b).

https://scholarworks.sjsu.edu/mcnair/vol19/iss1/9
DOI: 10.31979/mrj.2023.1909

(a) (b)

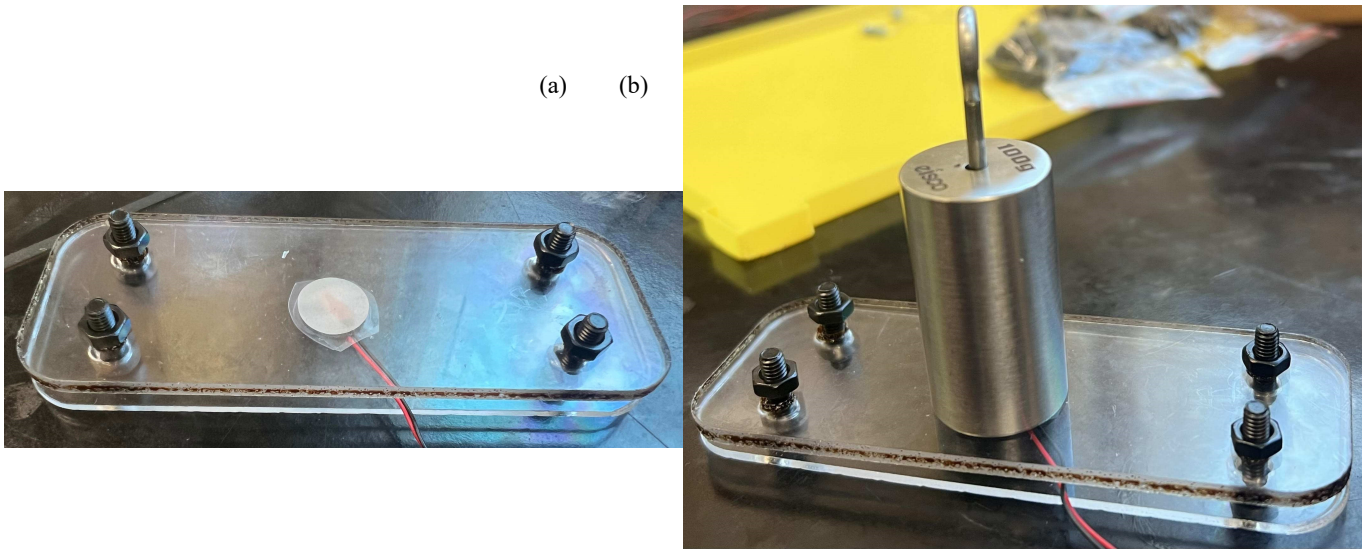

Fig. 14: Pressure sensor calibration apparatus (a) and apparatus with weight (b).

to follow a path vertically down the middle of the cylindrical-shaped sensor while the other end extends from the angular path of the spiral shape. The force sensor was 3D-printed with a conductive TPU filament called the NinjaTek Eel 3D printer filament to provide the conductive properties for force sensing. The sensor was printed with tree supports to realize the vertical spiral geometry when using the TPU filament.

Apparatus for pressure sensor calibration

An apparatus was designed to perform the pressure sensor calibration by placing various weights onto the pressure sensor. To stabilize the sensor in place and ensure control of the direct placement of the weight over the center of the pressure sensor, the sensor was placed between two acrylic plates. The plates were screwed to establish placement while being careful to minimize any excess pressure on the sensor from sandwiching the sensor between the two plates.

Apparatus for force sensor calibration

The apparatus for calibrating the force sensor was designed to perform testing that squeezes the vertical, cylindrical node at varying

weights. In this four-part design, the foundational piece has a notch for the circular part of the node to sit and allow the force sensor to sit horizontally. It also has a half-notch in a cylindrical shape for the stem of the node to sit in. The part that performs the squeezing has a top platform with another half-notch in a cylindrical shape and two cylindrical poles to sink down into two corresponding holes on the foundational component. Each pole also has a small hole to fit a toothpick through so that it can serve as a bar for hanging weights, causing the squeezing mechanism.

2.2 Mechatronic system for force and pressure feedback data

The mechatronic system to collect force and pressure data utilizes an Arduino MEGA microcontroller with the Arduino MEGA Sensor Shield v2.3 as displayed in figure 10 to collect voltage values through a serial data protocol. Each sensor is

Fig. 15: Apparatus for force sensor calibration.

https://scholarworks.sjsu.edu/mcnair/vol19/iss1/9
DOI: 10.31979/mrj.2023.1909

wired to a resistor to add a voltage divider to the system, with a resistance of 100 ohms used for the pressure sensor and 22 kilo-ohms for the force sensor. For each sensor, one end is connected to the black ground wire with copper tape and the other end is connected to the red power wire with copper tape as well. The red power wire is soldered to the resistor and to the yellow data wire before the resistor. The power supply is at 5 volts.

2.3 Sensor calibration

Pressure sensor calibration and analysis

Calibration was performed on six fabricated pressure sensors to analyze the static and dynamic response behavior, of which three would be chosen as the sensors for three pressure sensing nodes.

Using the calibration apparatus, weights were placed directly centered on top of the sensor within the acrylic plates to analyze the response to variations in pressure. The weights utilized were 100 g, 200 g, 300 g, 400 g, and 500 g. The process to perform the calibration included placing all five weights in order during one pass of calibration. Each weight was placed twice in a row before moving onto the next. The weight was placed on the sensor for 45 seconds and was removed to be left off of the sensor for 15 seconds before placing the next weight. As each weight was placed on and off of the sensor, the corresponding voltage values were collected through the Arduino IDE's serial monitor. Values were copied from the monitor and imported as a numeric matrix to MATLAB.

The first step of analyzing the data was to plot the raw voltage data versus time. The static analysis of the voltage data was performed by taking the average of the stable region for each weight's voltage readings. Then, the mass of each weight as the y-axis was plotted versus the average voltage as the x-axis for each weight. This plot was fit to a linear equation with an R^2 regression value. To obtain a final relation that converts voltage to pressure, an equation was developed from the linear-fit equation that demonstrates the relation between voltage and mass. The linear equation was written with 'y' as the mass and to account for the base voltage value, the input 'x', or the voltage, was subtracted by the base voltage. Using the standard pressure equation, shown in figure 16, the equation for mass

replaced the mass component to give a final conversion equation from voltage to pressure that is utilized in the live data processing method.

The dynamic analysis began with finding the rise time, or the time it took for the voltage value to increase back to the base voltage value after removing the weight. This was done by subtracting the corresponding times for the voltage value to go from 100% at the maximum voltage value to 0% at the base value. The drop time was calculated, which is the time it takes the voltage to drop to the final value after adding a weight. Of the values from the base voltage of the sensor to the maximum voltage value reached when a weight is placed, the drop time was calculated by subtracting the corresponding times from 10% to 90% of the range. By estimating from the plot of the raw voltage data, the initial drop time was calculated by subtracting the time at the base voltage from the time where the initial rapid drop in voltage after adding the weight begins to slow down. Using the voltage values at these two parts of the range, the corresponding percent of voltage drop out of the maximum voltage reached when placing the weight on the sensor was calculated.

The analyses of the six calibrated sensors were then compared to choose the final three sensors that would be used for the pressure sensing nodes. There were two primary factors considered in the comparison. One was the R^2 regression values and how close they were to a value of 1. The second factor was the dynamic time response data to see how quickly the sensors responded to adding and removing weights. This allowed for determining three sensors with the top performance.

$$P = \frac{m \times g}{A}$$

Fig. 16: Standard pressure equation where m = mass, g = gravitational constant, and A = cross-sectional area.

Force sensor calibration and analysis

A calibration method was developed to determine the static and dynamic behavior of the vertical force sensors while they are integrated into the silicone materials of various stiffnesses. The calibration process was

https://scholarworks.sjsu.edu/mcnair/vol19/iss1/9
DOI: 10.31979/mrj.2023.1909

performed twice on each of the three vertical sensors at two different orientations: one with the wiring attached to the sensor in the rightward horizontal direction and another with the wiring in the upright vertical direction to account for the asymmetry of the vertical sensor design. With the force sensor calibration apparatus, weights of 500 g, 750 g, 1000 g, 1250 g, and 1500 g were hung to provide various amounts of force through a squeezing mechanism. In a single pass of the calibration process, each weight was hung once in order from lowest to highest weight at 30 seconds hanging and 30 seconds for the node to recover after the weight is removed. Additionally, after all the weights were hung, data continued to be collected for an extra five minutes with no weight to collect data on the drop in voltage over time as it headed back toward the base voltage value. The voltage data was collected from the Arduino IDE and imported as a numeric matrix into MATLAB.

Analyzing the data began with plotting the raw voltage data against time for both the vertical and horizontal orientations. For static analysis, the average voltage was taken over the stable region for each weight. Then, the average voltages at each weight for the vertical and horizontal orientations were averaged to get one average value at each weight that takes into account the asymmetrical characteristic of the sensor design. These averaged voltage values were then plotted against mass, with mass on the y-axis and voltage on the x-axis. The plot was fit to a linear equation with an R^2 regression value. To get a final equation that converts voltage to force, the process begins by developing an equation from the linear-fit equation that relates mass to voltage. The linear equation was used to replace the 'y' component as the mass since it is located on the y-axis and to replace the 'x' component as the voltage that is on the x-axis. The voltage was also subtracted by the base voltage value of the force sensor. This equation for mass was then used to replace the mass component in the standard force equation in figure 18, which gives the final equation for the relationship between voltage and force that is used to calculate force in the live data processing.

Dynamic analysis of the force sensors was performed by analyzing two types of data. The first was calculating the average rise time, or the

average time it takes the voltage to increase to steady state once a weight is added. The second was the average drop percentage, which was the average percentage that the voltage drops relative to the base voltage during the 30-second period after a weight is removed.

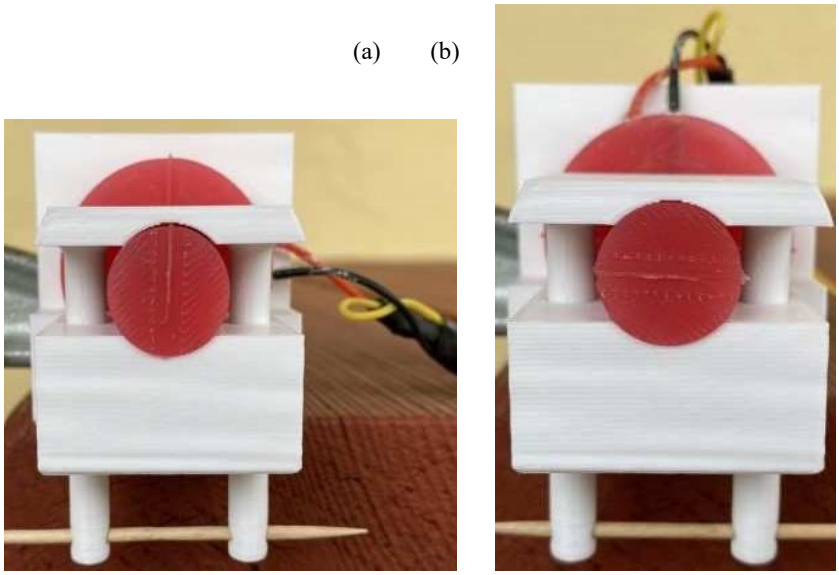

Fig. 17: Horizontal orientation of force sensor calibration apparatus (a) vertical orientation of apparatus (b).

$$F = mg$$

Fig. 18: Standard force equation where m = mass and g = gravitational constant.

https://scholarworks.sjsu.edu/mcnair/vol19/iss1/9
DOI: 10.31979/mrj.2023.1909

2.4 Live image processing with force and pressure mapping

The user interface within the surgical testbed apparatus encompasses a live video of the surgical pad with nodes overlaid with force and pressure mapping. This interface was developed in MATLAB. The live video feed was achieved through the looping of screenshots taken by a USB laparoscopic camera. Functions were created for each node in the video to be overlaid with a circle that changes color based on the range of force and pressure that the current value falls in. A colorbar was added to show the correspondence between the ranges of the force and pressure data values and their assigned colors. A box was added above each node that is color-coded to the dyed color of the node and provides the current force or pressure value.

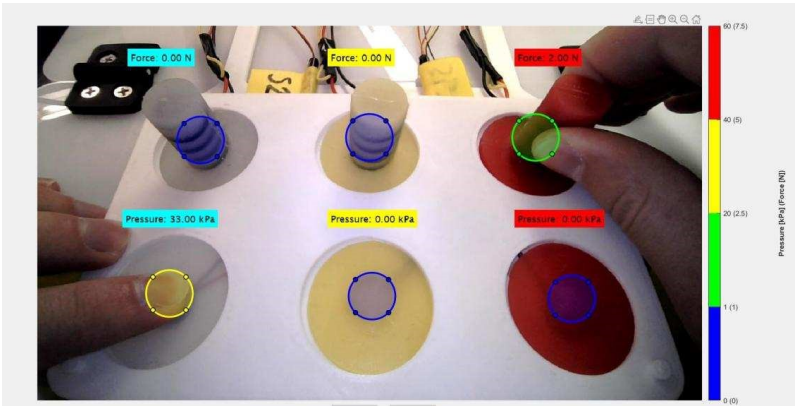

Fig. 19: User interface: live video overlaid with force and pressure mapping.

3 Results

3.1 Pressure sensor calibration and analysis

Figure 20 shows the raw data of voltage plotted against time for all six sensors throughout the calibration process. The base voltage for sensors 1-4 and sensor 6 are all around 5 V while the base voltage for sensor 5 is slightly lower at around 4.92 V. The addition of weight causes the drop in voltage and therefore, with increasing weight from 100 g to 500 g, the voltage progressively decreases. The pattern of decreasing in voltage

remained relatively consistent for the same weight amongst all six sensors with only slight variance, particularly in sensors 2, 3, and 5.

In figure 21, the plots contain the linearly fitted line and corresponding equation where y represents the mass and x represents the voltage. Each plot also has an R^2 regression value. The plots for all 6 sensors exhibited a common pattern where the average voltage values at each mass followed a generally linear trend. This is shown not only by the linearly fit line, but by the R^2 values, which are all very close to 1.

Table 2 shows the dynamic response data of all six sensors. The rise in voltage when the weight was removed occurred the fastest, particularly in comparison to the drop time when the weight was added, which was much slower. Although the drop time was relatively longer, the drop in voltage reached between 72% and 84% of its final value within a very short time that is comparable to the rise time. Amongst the six sensors, sensors 1, 2, and 6 had the fastest responses, but all six sensors were fairly consistent and within a similar range to each other.

In comparing the linear trends of the six sensors and their dynamic time responses, the sensors that showed the best balance of these characteristics were sensors 2, 4, and 5. They all had a linear fit with an R^2 value of at least 0.98 while maintaining relatively fast dynamic responses. For instance, the rise times for sensors 2, 4 and 5 were around 0.16 seconds, 0.25 seconds, and 0.22 seconds, respectively. Sensor 4 had a reasonable drop time of around 3.4 seconds and second-largest initial drop of 82.84%. Therefore, sensors 2, 4 and 5 were the sensors chosen out of the six calibrated sensors to be utilized in the pressure sensing nodes. The equations developed to convert voltage to pressure by using the methodology previously described are shown in figure 22.

https://scholarworks.sjsu.edu/mcnair/vol19/iss1/9
DOI: 10.31979/mrj.2023.1909

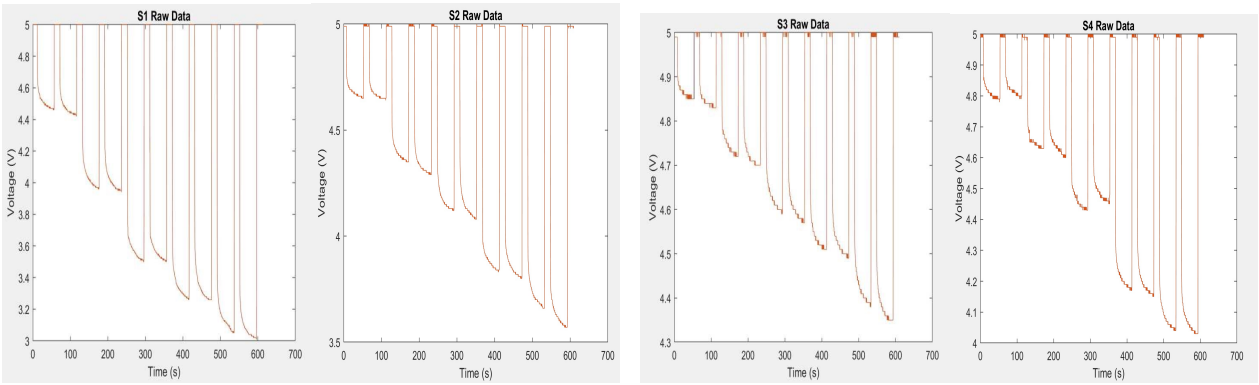

(a) (b) (c) (d)

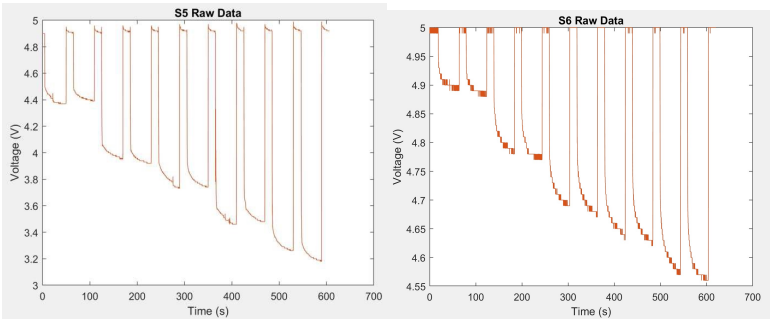

(e) (f)

Fig. 20: Raw voltage data plotted against time for sensor 1 (a), sensor 2 (b), sensor 3 (c), sensor 4 (d), sensor 5 (e), and sensor 6 (f).

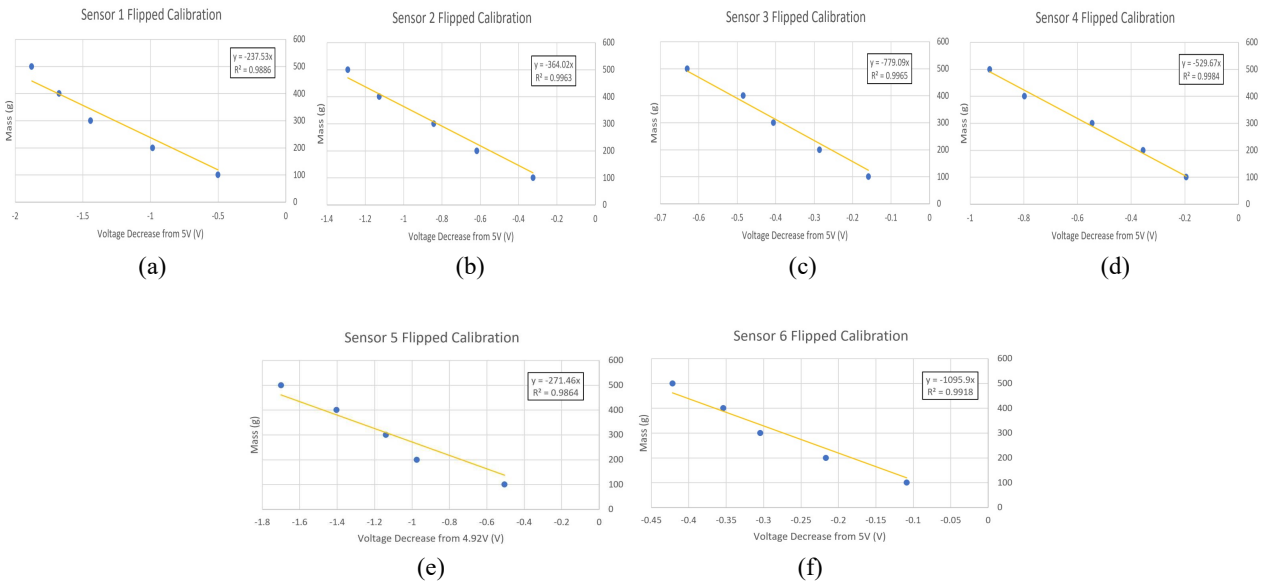

Fig. 21: Linearly fitted plots of mass versus voltage for sensor 1 (a), sensor 2 (b), sensor 3 (c), sensor 4 (d), sensor 5 (e), and sensor 6 (f).

3.2 Force sensor calibration and analysis

Raw data of the changes in voltage over time in both the vertical and horizontal orientations is shown in figure 23. Unlike the pressure sensors, as weight is added to squeeze the force sensor, the voltage increases rather than decreases. Another distinction is that each time a new weight was added, which is shown by each peak on the plots, the sensors were not able to return all the way back to the base voltage value during the rest period before the next weight was added. Even after waiting five minutes with no weight at the end of the calibration process, the voltage greatly reduced, but was not able to fully return to the base voltage value.

Between the calibration tests performed at the vertical and horizontal orientations, the average voltage values at each weight were averaged and plotted as the x-axis against the mass on the y-axis. While all three force sensors at various silicone stiffnesses had a linear trend for the change in voltage at different weights, the sensors in the fat-like and glandular-like silicone tissues showed the best fit, including the highest R^2 values that are over 0.99. Even so, the sensor embedded in the vascular-like

https://scholarworks.sjsu.edu/mcnair/vol19/iss1/9
DOI: 10.31979/mrj.2023.1909

Table 2: Dynamic Time Response Data for Pressure Sensors.

Sensor	Rise Time (Weight Removed) [s]	Drop Time (Weight Added) [s]	Initial Drop Time [s]	Initial Drop [%]
S1	0.1968	3.2016	0.6556	78.21
S2	0.1638	3.0248	0.5420	78.56
S3	0.2046	4.0948	0.6650	77.64
S4	0.2516	3.4038	0.8236	82.84
S5	0.2188	1.6470	0.8208	84.02
S6	0.1580	4.8556	0.7458	72.94

$$P = (v - 5) \times -28.19 \quad \text{(a)}$$

$$P = (v - 5) \times -41.02 \quad \text{(b)}$$

$$P = (v - 4.92) \times -21.02 \quad \text{(c)}$$

Fig. 22: Equations to convert voltage to pressure for sensor 2 (a), sensor 4 (b), and sensor 5 (c) where v = voltage [V] and P = pressure [kPa].

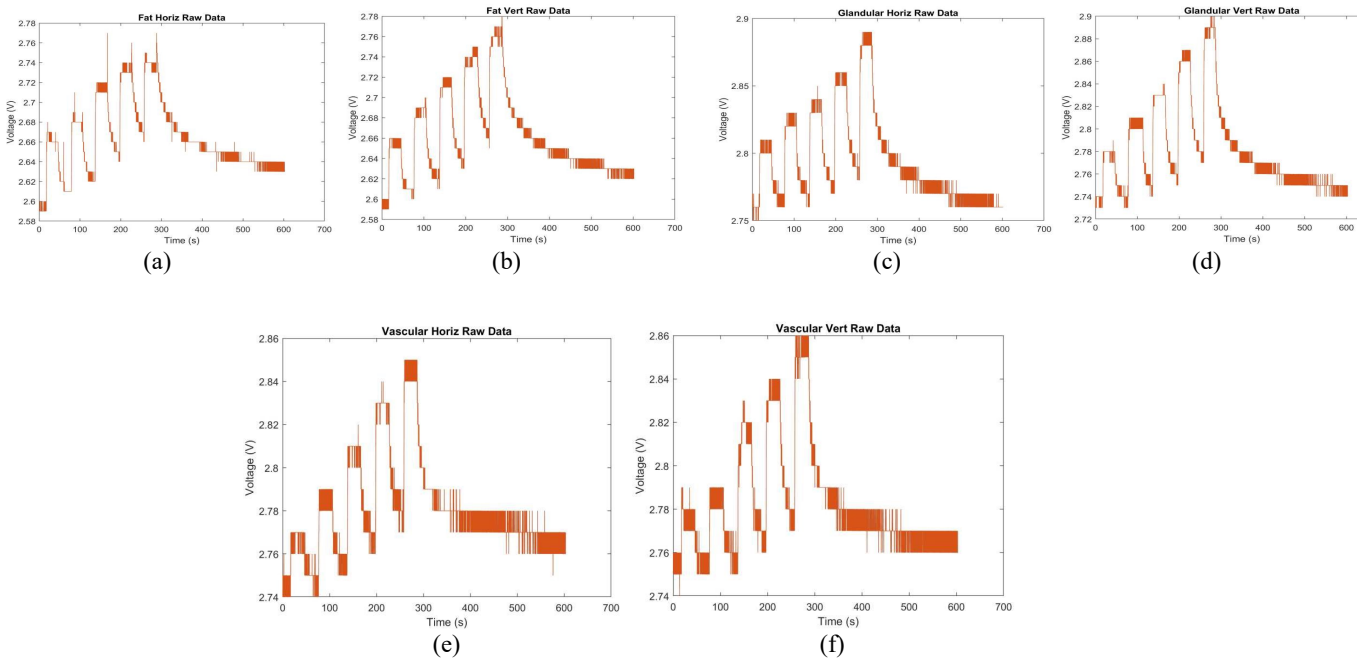

Fig. 23: Plots of raw voltage data versus time for the horizontal orientation of sensor 1 (a), sensor 2 (b), and sensor 3 (c), and for the vertical orientation of sensor 1 (d), sensor 2 (e), and sensor 3 (f).

tissue gave a linear fit with a high R^2 value of at least 0.98. The slight variation between the three force sensors is acceptable since a separate equation for converting voltage to force is made for each one.

In table 3, the average rise time and average drop percentages are compared amongst the three sensors embedded in varying tissue stiffnesses. The sensor in vascular-like tissue took only about around 0.5 seconds to reach the steady state after adding a weight while the sensors in the fat-like and glandular-like tissue took almost double that time. In terms of the average drop percentage, the sensor in fat-like tissue had the lowest drop at 64.73% of the base voltage value after 30 seconds of the weight being removed, while the sensors in glandular-like and vascular-like tissue were more improved at drops of around 76% of the base voltage value.

In the case of the force sensors, three sensors were fabricated and embedded in the three different stiffnesses of silicone tissue. With no

https://scholarworks.sjsu.edu/mcnair/vol19/iss1/9
DOI: 10.31979/mrj.2023.1909

selection process, all three sensors are used in the three force sensing nodes. The static and dynamic character-

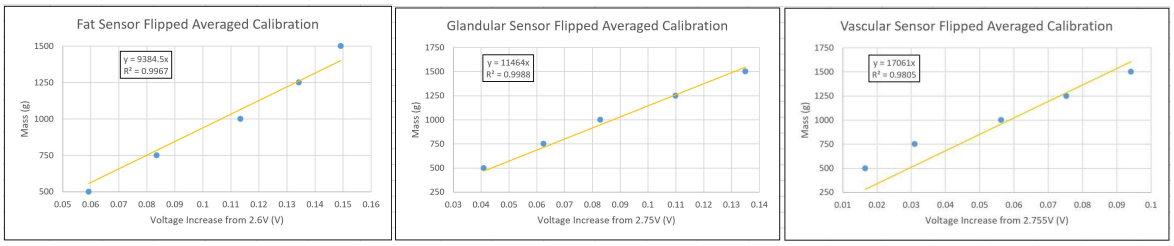

(a) (b) (c)

Fig. 24: Linearly-fitted plots of mass versus voltage for the sensors embedded in fat-like (a), glandular-Like (b), and vascularlike (c) silicone tissue.

Table 3: Dynamic Time Response Data for Force Sensors Embedded in Silicone.

Tissue	Average Rise Time [s]	Average Drop [%]
Fat	0.9707	64.73
Glandular	0.9672	76.45
Vascular	0.4972	76.95

$$F = (v - 2.46) \times 140.14$$ (a)

$$F = (v - 2.65) \times 99.09$$ (b)

$$F = (v - 2.65) \times 169.14$$ (c)

Fig. 25: Equations to convert voltage to force for sensors embedded in fat-like (a), glandular-Like (b), and vascular-like (c) silicone tissue where v = voltage [V] and F = force [N].

istics of each sensor were reasonably accepted and the methodology previously described was used to develop an equation that converts voltage to force for each sensor, as shown in the equations in figure 25. However, accuracy in returning to the base voltage value and improving response characteristics exhibits room for improvement.

4 Discussion

4.1 Pressure sensors

For each pressure sensor, the changes in voltage at each weight progressed consistently so that if the same weight was applied twice in a row, it reached just about the same drop in voltage. While this was consistent with the patterns of each individual sensor, comparing the sensors' raw data to each other shows some variance in the drop in voltage associated with each weight. This is acceptable in our application because each weight is calibrated separately to obtain an equation for each sensor that will be used to convert voltage to pressure.

In determining the top three pressure sensors to be used in the pressure sensing nodes, both the static and dynamic results were utilized. Sensors 2, 4, and 5 were selected because they exhibited the highest R^2 values that are over 0.98 while also maintaining relatively fast dynamic responses and large initial drop percentages. Any variations in data amongst the pressure sensors are evidence of some variation in the fabrication that took place by-hand despite following an identical process. This reflection does not hold a significant negative impact on the final equation that is utilized to convert voltage to pressure and more specifically, on the sensors' usage in the testbed apparatus. This is because all of the sensors are within the same relative range to where the slight variance does not hold weight in the overall performance of the testbed as long as there is an equation for each sensor rather than one equation that can apply to all of the sensors.

4.2 Force sensors

During the calibration process, the force sensors exhibited a unique behavior where the voltage was not able to reach the base voltage even after 30 seconds with no weight. Further, after five minutes with no weight at the end of the tests, the voltage was still not able to be reduced all the way down

https://scholarworks.sjsu.edu/mcnair/vol19/iss1/9
DOI: 10.31979/mrj.2023.1909

to the base voltage. This could mean that it would take even more time to reach the base voltage than allotted in the current methodology, but longer time between interactions is not efficient for the real-time interactions necessary in the MIS training processes. The behavior seems to result from multiple factors. Since the force sensors are embedded in the silicone tissue, this may be slowing down the response after removing weight from the sensor. Additionally, the conductive filament used to print the force sensor may be experiencing effects of slight permanent deformation throughout the calibration process. In general, the material properties and behavior of the silicone and especially the conductive filament may require more advanced materials studies to fully understand this behavior. For the purposes of the surgical testbed, the prototype is reasonably functional with the equations developed through the current methodology. However, the accuracy and reliability of the force sensors is needed to be improved through further testing of material properties and further improvements to the calibration process based on these results.

5 Conclusion

The cost-effective, smart-sensing surgical testbed fulfills a clinical need for accessible and effective training in minimally invasive surgery. The pressure and force feedback during testbed interaction is a novel feature that is not yet commercially available, but is important to the motor skills and intuitive sensing practiced by surgeons in training. Additionally, the interaction with various tissue stiffnesses such as tissue comparable to fat, glandular, and vascular tissue, is vital to providing MIS trainees with experience in interacting with various levels of tissue stiffnesses in the human body. While providing these features is a leap forward amongst the box trainers currently on the market, modified pressure sensor fabrication techniques can improve the consistency amongst the pressure sensors and further material experimentation as well as calibration process adjustment is needed to improve the accuracy of the force sensors.

6 Future work

Following the development of the smart-sensing surgical testbed, this apparatus is planned to be integrated into a telesurgical robotic training system. In conjunction with a robotic gripper added to a robot, the goal of this future work is to characterize the human-centric metrics and model the human operator's behavior. More specifically, this study aims to evaluate the operator's ability to control the moving end effector and manipulate tools to grasp tissue from a laparoscopic surgical training module using Fitts' Law.

Acknowledgements

This work is supported by the Small Group Project Award in the College of Engineering at San Jose State University. We would like to express our deepest gratitude to Dr. Lin Jiang for proposing this project. She has been instrumental in our project development, offering us critical guidance, ideas, and feedback about our prototype designs and overall progress. Additionally, we sincerely thank the McNair Scholars Program for sponsoring portions of this project.

We are also grateful to Dr. Hussameddine Kabbani for ensuring that we are on track to make good progress. We would also like to express our gratitude to Jenny Huynh for providing us with resources for literature review on robotic surgery, as well as sharing details and a 3D model of her gripper design which will interact with our project. We would like to thank Melissa Ng for teaching and guiding us through the process of pouring and curing silicone and for sharing advice on improving our mold designs. Finally, we would like to thank Jonathan Lim for his assistance in 3D-printing the force sensors.

References

[1] Vitiello, V., Lee, S.-L., Cundy, T. P., and Yang, G.-Z., 2012. "Emerging robotic platforms for minimally invasive surgery". *IEEE reviews in biomedical engineering,* 6, pp. 111–126.

[2] Lahanas, V., Georgiou, E., and Loukas, C., 2016. "Surgical simulation training systems: box trainers, virtual reality and augmented reality

https://scholarworks.sjsu.edu/mcnair/vol19/iss1/9
DOI: 10.31979/mrj.2023.1909

simulators". *International Journal of Advanced Robotics and Automation,* 1(2), pp. 1–9.

[3] Casarin, J., Multinu, F., Ubl, D. S., Dowdy, S. C., Cliby, W. A., Glaser, G. E., Butler, K. A., Ghezzi, F., Habermann, E. B., and Mariani, A., 2018. "Adoption of minimally invasive surgery and decrease in surgical morbidity for endometrial cancer treatment in the united states". *Obstetrics & Gynecology,* 131(2), pp. 304–311.

[4] Daly, S. C., Popoff, A. M., Fogg, L., Francescatti, A. B., Myers, J. A., Millikan, K. W., Deziel, D. J., and Luu, M. B., 2014. "Minimally invasive technique leads to decreased morbidity and mortality in small bowel resections compared to an open technique: an acs-nsqip identified target for improvement". *Journal of Gastrointestinal Surgery,* 18(6), pp. 1171–1175.

[5] Li, M. M., and George, J., 2017. "A systematic review of low-cost laparoscopic simulators". *Surgical endoscopy,* 31(1), pp. 38–48.

[6] Jade, H. Laparoscopy.

[7] limbs amp; things: closer to life. User guide: Fundamentals of laparoscopic surgery trainer system amp; accessories.

[8] fls: limbs amp; things. Fls trainer system.

[9] aliexpress. Laparoscopic simulator training box foldable laparoscopy endo trainer medical teaching equipment.

[10] fls: limbs amp; things. Fls trainer box with tv camera.

[11] 3b scientific. Lap-x box laparoscopy trainer.

[12] 3b scientific. Lap-x vr.

[13] Horeman, T., Rodrigues, S. P., van den Dobbelsteen, J. J., Jansen, F.-W., and Dankelman, J., 2012. "Visual force feedback in laparoscopic training". *Surgical endoscopy,* 26(1), pp. 242–248.

[14] Horeman, T., Rodrigues, S. P., Jansen, F.-W., Dankelman, J., and van den Dobbelsteen, J. J., 2010. "Force measurement platform for training and assessment of laparoscopic skills". *Surgical endoscopy,* 24(12), pp. 3102–3108.

[15] Partridge, R., Hughes, M., Brennan, P., and Hennessey, I., 2015. "There is a worldwide shortfall of simulation platforms for minimally invasive surgery". *JSS,* 2, pp. 12–7.

[16] Li, Y., Liu, K., He, W., Yin, Y., Johansson, R., and Zhang, K., 2019. "Bilateral teleoperation of multiple robots under scheduling communication". *IEEE Transactions on Control Systems Technology,* 28(5), pp. 1770–1784.

[17] Xu, W., Peng, J., Liang, B., and Mu, Z., 2016. "Hybrid modeling and analysis method for dynamic coupling of space robots". *IEEE Transactions on Aerospace and Electronic Systems,* 52(1), pp. 85–98.

[18] Okamura, A. M., Mataric, M. J., and Christensen, H. I., 2010. "Medical and health-care robotics".´ *IEEE Robotics & Automation Magazine,* 17(3), pp. 26–37.

[19] Di Natali, C., Buzzi, J., Garbin, N., Beccani, M., and Valdastri, P., 2015. "Closed-loop control of local magnetic actuation for robotic surgical instruments". *IEEE Transactions on Robotics,* 31(1), pp. 143–156.

[20] Niemeyer, G., and Slotine, J.-J., 1991. "Stable adaptive teleoperation". *IEEE Journal of oceanic engineering,* 16(1), pp. 152–162.

[21] Ryu, J.-H., Kwon, D.-S., and Hannaford, B., 2004. "Stable teleoperation with time-domain passivity control". *IEEE Transactions on robotics and automation,* 20(2), pp. 365–373.

[22] Chan, L., Naghdy, F., and Stirling, D., 2014. "Application of adaptive controllers in teleoperation systems: A survey". *IEEE Transactions on Human-Machine Systems,* 44(3), pp. 337–352.

[23] Luo, J., Yang, C., Li, Q., and Wang, M., 2019. "A task learning mechanism for the telerobots". *International Journal of Humanoid Robotics,* 16(02), p. 1950009.

[24] Palep, J. H., 2009. "Robotic assisted minimally invasive surgery". *Journal of minimal access surgery,* 5(1), p. 1.

[25] Okamura, A. M., 2009. "Haptic feedback in robot-assisted minimally invasive surgery". *Current opinion in urology,* 19(1), p. 102.

https://scholarworks.sjsu.edu/mcnair/vol19/iss1/9
DOI: 10.31979/mrj.2023.1909

[26] Kneebone, R., 2003. "Simulation in surgical training: educational issues and practical implications". *Medical education,* 37(3), pp. 267–277.

[27] Kowalewski, K.-F., Schmidt, M. W., Proctor, T., Pohl, M., Wennberg, E., Karadza, E., Romero, P., Kenngott, H. G., Muller-Stich, B. P., and Nickel, F., 2018. "Skills in minimally invasive and open surgery show limited transferability to¨ robotic surgery: results from a prospective study". *Surgical Endoscopy,* 32(4), pp. 1656–1667.

[28] Samani, A., Zubovits, J., and Plewes, D., 2007. "Elastic moduli of normal and pathological human breast tissues: an inversion-technique-based investigation of 169 samples". *Physics in medicine & biology,* 52(6), p. 1565.

[29] L.M. Cannon et al., 2011. "Novel tissue mimicking materials for high frequency breast ultrasound phantoms". *Ultrasound Med. Biol.,* 37(1), pp. 122–135.

[30] Chanda, A., 2018. "Biomechanical modeling of human skin tissue surrogates". *Biomimetics,* 3(3), p. 18.